Journal of Engineering for Gas Turbines and Power

Copy of e-mail Notification

Journal of Engineering for Gas Turbines and Power Published by ASME
Dear Author,

Congratulations on having your paper accepted for publication in the ASME Journal Program.
Your page proof is available from the ASME Proof site here:
http://cps.kwglobal.com/MIS/AuthorProofLogin.aspx?pwd=16ff383879de&CA=AS

Login: your e-mail address
Password: 16ff383879de

Please keep this email in case you need to refer back to it in the future.

Responsibility of detecting errors rests with the author. Please review the page proofs carefully and:
1. Answer any queries on the “Author Query Form”
2. Proofread any tables and equations carefully
3. Check to see that any special characters have translated correctly
4. Publication will not proceed until a response is received. If there are no corrections, a response is still required.

RETURNING CORRECTIONS:
Corrections must be returned using the ASME Proof Download & Corrections Submission Site (link above). You will be able to upload:
1. Annotated PDF
2. Text entry of corrections, with line numbers, in the text box provided
3. Additional files, if necessary.

SPECIAL NOTES:
Your Login and Password are valid for a limited time. Please reply within 48 hours.

Corrections not returned through the above website will be subject to publication delays.
This e-proof is to be used only for the purpose of returning corrections to the publisher.
If you have any questions, please contact: asme.cenveo@cenveo.com, and include your article no. (GTP-17-1443) in the subject line. This email should not be used to return corrections.

Approval of these proofs re-confirms the copyright agreement provision that all necessary rights from third parties for any copyrighted material (including without limitation any diagrams, photographs, figures or text) contained in the paper has been obtained in writing and that appropriate credit has been included.

Sincerely,
Mary O'Brien, Journal Production Manager

STATEMENT OF EDITORIAL POLICY AND PRACTICE

The Technical Committee on Publications and Communications (TCPC) of ASME aims to maintain a high degree of technical, literary, and typographical excellence in its publications. Primary consideration in conducting the publications is therefore given to the interests of the reader and to safeguarding the prestige of the Society.

To this end the TCPC confidently expects that sponsor groups will subject every paper recommended by them for publication to careful and critical review for the purpose of eliminating and correcting errors and suggesting ways in which the paper may be improved as to clarity and conciseness of expression, accuracy of statement, and omission of unnecessary and irrelevant material. The primary responsibility for the technical quality of the papers rests with the sponsor groups.

In approving a paper for publication, however, the TCPC reserves the right to submit it for further review to competent critics of its own choosing if it feels that this additional precaution is desirable. The TCPC also reserves the right to request revision or condensation of a paper by the author or by the staff for approval by the author. It reserves the right, and charges the editorial staff, to eliminate or modify statements in the paper that appear to be not in good taste and hence likely to offend readers (such as obvious advertising of commercial ventures and products, comments on the intentions, character, or acts of persons and organizations that may be construed as offensive or libelous), and to suggest to authors rephrasing of sentences where this will be in the interest of clarity. Such rephrasing is kept to a minimum.

Inasmuch as specific criteria for the judging of individual cases cannot, in the opinion of the TCPC, be set up in any but the most general rules, the TCPC relies upon the editorial staff to exercise its judgment in making changes in manuscripts, in rearranging and condensing papers, and in making suggestions to authors. The TCPC realizes that the opinions of author and editor may sometimes differ, and hence it is an invariable practice that no paper is published until it has been passed on by the author. For this purpose page proofs of the edited paper are sent to the author prior to publication in a journal. Changes in content and form made in the proofs by authors are followed by the editor except in cases in which the Society's standard spelling and abbreviation forms are affected.

If important differences of opinion arise between author and editor, the points at issue are discussed in correspondence or interview, and if a solution satisfactory to both author and editor is not reached, the matter is laid before the TCPC for adjustment.

Technical Committee on Publications and Communications (TCPC)
Reviewed: 05/2012

AUTHOR QUERY FORM

ASME SETTING THE STANDARD	**Journal: J. Eng. Gas Turbines Power** **Article Number: GTP-17-1443**	**Please provide your responses and any corrections by annotating this PDF and uploading it to ASME's eProof website as detailed in the Welcome email.**

Dear Author,

Below are the queries associated with your article; please answer all of these queries before sending the proof back to Cenveo. Production and publication of your paper will continue after you return corrections or respond that there are no additional corrections.

Location in article	Query / Remark: click on the Q link to navigate to the appropriate spot in the proof. There, insert your comments as a PDF annotation.
AQ1	Reminder – the ASME Copyright Agreement that was signed by all authors includes the following: "You have the right to enter into this Copyright Form and to make the assignment of rights to ASME. If the Paper contains excerpts from other copyrighted material (including without limitation any diagrams, photographs, figures or text), you have acquired in writing all necessary rights from third parties to include those materials in the Paper, and have provided appropriate credit for that third-party material in footnotes or in a bibliography." As required, ASME may contact the authors to obtain a copy of the written permission.
AQ2	Any content obtained from the web and included in the paper may require written permission and appropriate credit if it is copyrighted content. If copyright status cannot be determined, this content should not be included in the paper.
AQ3	As per journal style, three or fewer letters acronyms are not allowed in the title; therefore, we have replaced the acronym CFD with the spelled out definition.
AQ4	Please check and confirm the presentation of hierarch.
AQ5	Please define CAD at first occurrence.
AQ6	As per style italic for the terms has been retained in the first occurrence and removed from the subsequent occurrence. Kindly check and confirm.
AQ7	Please provide page range/paper number for Ref. 2.
AQ8	Please provide page number in range and confirm the presentation for Ref. 26.
AQ9	Please provide DOI or website to access article for Ref(s). 6, 14, 25, 29–31.

Thank you for your assistance.

PROOF COPY [GTP-17-1443]

AQ1
AQ2

Quantitative Computational Fluid Dynamics Analyses of Particle Deposition in a Heavy-Duty Subsonic Axial Compressor

Nicola Aldi[1]
Dipartimento di Ingegneria,
Università degli Studi di Ferrara,
AQ3 Ferrara 44122, Italy

Nicola Casari
Dipartimento di Ingegneria,
Università degli Studi di Ferrara,
Ferrara 44122, Italy

Devid Dainese
Dipartimento di Ingegneria,
Università degli Studi di Ferrara,
Ferrara 44122, Italy

Mirko Morini
Dipartimento di Ingegneria e Architettura,
Università degli Studi di Parma,
Parma 43121, Italy

Michele Pinelli
Dipartimento di Ingegneria,
Università degli Studi di Ferrara,
Ferrara 44122, Italy

Pier Ruggero Spina
Dipartimento di Ingegneria,
Università degli Studi di Ferrara,
Ferrara 44122, Italy

Alessio Suman
Dipartimento di Ingegneria,
Università degli Studi di Ferrara,
Ferrara 44122, Italy

Solid particle ingestion is one of the principal degradation mechanisms in the compressor and turbine sections of gas turbines. In particular, in industrial applications, the microparticles not captured by the air filtration system can cause deposits on blading and, consequently, result in a decrease in compressor performance. In the literature, there are some studies related to the fouling phenomena in transonic compressors, but in industrial applications (heavy-duty compressors, pump stations, etc.), the subsonic compressors are widespread. It is highly important for the manufacturer to gather information about the fouling phenomenon related to this type of compressor. This paper presents three-dimensional (3D) numerical simulations of the microparticle ingestion (0.15–1.50 μm) in a multistage (i.e., eight stage) subsonic axial compressor, carried out by means of a commercial computational fluid dynamic code. Particles of this size can follow the main air flow with relatively little slip, while being impacted by flow turbulence. It is of great interest to the industry to determine which zones of the compressor blades are impacted by these small particles. Particle trajectory simulations use a stochastic Lagrangian tracking method that solves the equations of motion separately from the continuous phase. The adopted computational strategy allows the evaluation of particle deposition in a multistage axial compressor thanks to the use of a mixing plane approach to model the rotor/stator interaction. The compressor numerical model and the discrete phase model are set up and validated against the experimental and numerical data available in the literature. The number of particles and sizes is specified in order to perform a quantitative analysis of the particle impacts on the blade surface. The blade zones affected by particle impacts and the kinematic characteristics (velocity and angle) of the impact of micrometric and submicrometric particles with the blade surface are shown. Both blade zones affected by particle impact and deposition are analyzed. The particle deposition is established by using the quantity called sticking probability, adopted from the literature. The sticking probability links the kinematic characteristics of particle impact on the blade with the fouling phenomenon. The results show that microparticles tend to follow the flow by impacting on the compressor blades at full span. The suction side of the blade is only affected by the impacts of the smallest particles. Particular fluid dynamic phenomena, such as corner separations and clearance vortices, strongly influence the impact location of the particles. The impact and deposition trends decrease according to the stages. The front stages appear more affected by particle impact and deposition than the rear ones.
[DOI: 10.1115/1.4038608]

AQ4

Introduction

Land-based gas turbine operation is affected by the fouling phenomenon that afflicts both compressor and turbine sections. Studies and analyses related to fouling have grown continuously over the years due to the necessity of increasing the performance, efficiency, and reliability of gas turbines [1].

Compressor fouling is primarily due to the microparticles ingested by the power unit. Microparticles are able to pass through the filtration barriers and stick to the compressor surfaces [2,3]. The mechanisms through which this adhesion occurs are still not fully understood. A rule-of-thumb in the literature highlights that dry particles have to be very small to stick, while wet surfaces and/or wet particles allow bigger particles to stick [2]. Deposits along the gas path determine a reduction in compressor performance and efficiency. As reported in Refs. [4] and [5], the reduction in compressor performance due to fouling depends on the severity of the phenomenon, whose occurrence is modeled through a decrease in the flow passage area and efficiency.

Multistage compressors experience several different phenomena related to fouling. Flow conditions (such as temperature and pressure) change through the stages. On-field detections [6,7] reveal particular contamination patterns and different amounts of deposits.

Tarabrin et al. [6] report an investigation of compressor blade contamination for a Nuovo Pignone MS5322 R(B) gas turbine engine. This power unit operated for a long time without blade washing, but only the first 5–6 stages of 16 are subjected to fouling. Figure 1 shows the results of the author's inspection. The inlet guide vanes, as well as rotor blades and stator vanes of the first stage, have more deposits on the convex side. The deposit masses on the blades of the other stages are approximately equal for the convex and concave sides, with deposit masses decreasing from the first to the sixth stage. The authors point out that the amount of deposits is greater on stator vanes than on rotor blades due to the cleaning effects provided by centrifugal forces on dirt particles. Centrifugal force effects also influence the results

[1]Corresponding author.

Contributed by the Turbomachinery Committee of ASME for publication in the Journal of Engineering for Gas Turbines and Power. Manuscript received August 9, 2017; final manuscript received September 21, 2017; published online xx xx, xxxx. Editor: David Wisler.

obtained by Syverud et al. [7]. The authors report the location of salt deposits in a general electric J85-13 axial compressor. The experimental tests show that salt deposits are mainly found along the leading edge of the first four stages and on the pressure side of stator vanes along the hub. According to the author's inspection, deposits are mainly located on the leading edge of stator vanes. Close to the hub, some of the deposits were detached by the air flow probably due to the variation of the incident angle when the compressor was tested at a different rotational speed. The salt deposits were generated by the salt carried by the water droplets and, for this reason, significantly fewer deposits are observed on rotor blades compared to stator vanes due to the centrifugal forces.

Numerical analyses of the fouling phenomenon in multistage compressors are not widespread in the literature and some studies have only become available in the last few years. The challenges involved in these types of simulations are linked to particle size (submicrometric particles) and computational efforts. Examples of computational fluid dynamics (CFD) analyses of the particle ingestion in axial-flow compressors can be found in Refs. [8] and [9]. In these works, which deal with compressor erosion, particle trajectories are investigated in order to reveal the main eroded areas of the blades. In Ref. [10], Aldi et al. analyze the microparticle ingestion in a transonic axial compressor stage. A particular computational strategy is adopted to take into account the presence of two subsequent annular cascades. Recently, Saxena et al. [11] have performed a numerical study of a high-pressure axial compressor ingesting particulate matter, in order to predict particle behavior both along the stages and the compressor bleed system. The effect of particle shape is also studied by simulating nonspherical particles.

Compressor Numerical Model

The compressor under examination is an eight-stage subsonic axial-flow compressor used in an industrial application. The compressor overall axial length is 0.934 m. It is characterized by a constant hub diameter annulus configuration, with the hub diameter of 0.480 m and the casing diameter linearly decreasing along the axial direction from 0.650 m at the first rotor inlet to 0.578 m at the last stator exit. Each rotor consists of 31 blades, while each stator is composed of 44 vanes. The rotor tip and the stator hub clearances are equal to 0.382 mm for all cascades. The compressor design rotational speed is 6054 rpm and the first rotor blade tip speed is equal to 206 m/s, which corresponds to a blade tip Mach number of 0.62.

Computational Domain. The compressor geometry is reconstructed through a reverse engineering procedure. The geometry reconstruction of the real components is performed by means of a laser scanner. At first, a three-dimensional (3D) polygonal geometry of the actual geometry is obtained by interpolating the point cloud derived from the laser scanner by means of POLYWORKS V12 software. A 3D model is then obtained and exported to the CAD software SOLIDWORKS 2015 through an interchange file format. A sketch of the computational domain for the compressor is shown in Fig. 2(*a*). As can be seen, the computational domain consists of eighteen fluid domains: ten stationary domains (inlet duct, stators, and outlet duct) and eight rotating domains (rotors). To reduce the computational effort, only a single passage per cascade is modeled. AQ5

Numerical Grid. The grid used in the calculations is a hexahedral grid with a total number of 16,594,824 elements. The grid is realized by employing an O-grid around both rotor blades and stator vanes, with local refinements near the hub and shroud regions. Rotor tip and stator hub clearances are resolved with 4 nodes across the gap span. The meshes on a single rotor blade and stator vane are shown in Figs. 2(*b*) and 2(*c*), respectively. The first grid points on rotor blades, stator vanes, and end walls are positioned in such a way that the y^+ values range from 10 to 250.

Numerical Code. The numerical simulations are carried out by means of the commercial CFD code ANSYS CFX 16.2. The code solves the 3D Reynolds-averaged form of the Navier–Stokes equations by using a finite element-based finite volume method. An algebraic multigrid method, based on the additive correction multigrid strategy, is used. A second-order high-resolution advection scheme is adopted to calculate the advection terms in the flow equations.

Turbulence Model. The turbulence model used in the calculations is the standard k–ε and near-wall effects are modeled by means of scalable wall functions [12]. A first-order upwind discretization scheme is selected for both turbulent kinetic energy and turbulent dissipation rate equation.

Rotor/Stator Interaction Model. All the compressor simulations are performed in a steady multiple reference frame in order to take into account the contemporary presence of moving and stationary domains. In particular, a mixing plane model is imposed at the interface between rotating and stationary domains, each of

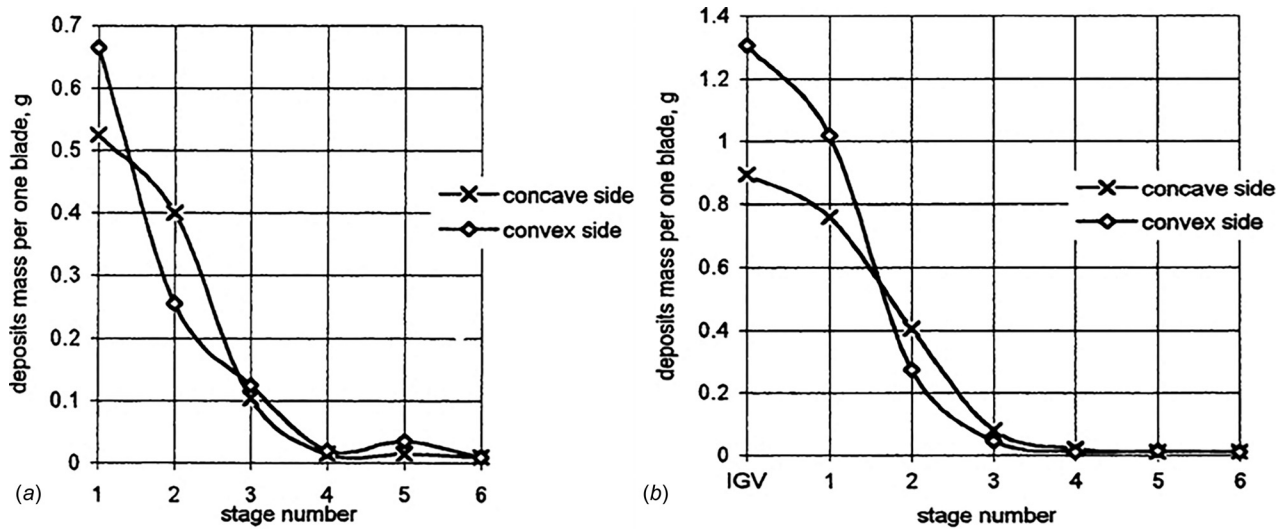

Fig. 1 Weight distribution of deposits on the convex and concave sides of the compressor blades [6]: (*a*) rotors and (*b*) stators

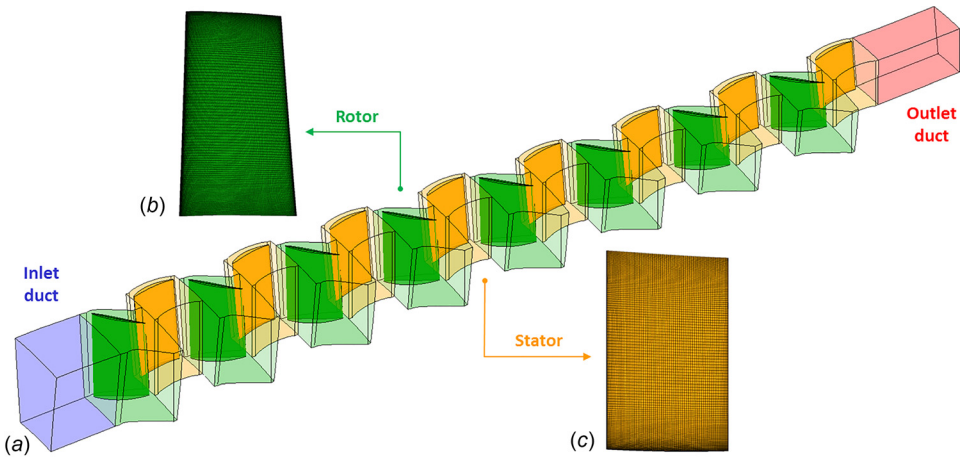

Fig. 2 Computational domain for the multistage compressor: (*a*) single passage model, (*b*) mesh on a rotor blade, and (*c*) mesh on a stator vane

which is solved as a steady-state problem. The mixing plane interface, whose geometry is radial, is located half-way between the two cascades.

In Ref. [13], Cornelius et al. carry out a numerical analysis on a six-stage axial compressor using both steady mixing plane and transient methods for the rotor/stator interaction. All the simulations show strong agreement with the experimental data across the full performance map, up to stall onset on multiple speedlines. From these analyses, it can be seen that the steady simulation with a mixing plane approach is reliable in reproducing the overall performance of the compressor, avoiding the more expensive (in terms of time and computational effort) transient approach.

Properties and Boundary Conditions. An ideal gas approximation is used for air. It is also assumed that the fluid has a constant specific heat, dynamic viscosity, and thermal conductivity.

The total pressure, the total temperature, and the flow direction are assigned to the inflow boundary of the inlet duct. The inlet total pressure $p_{0,\mathrm{in}}$ and the total temperature $T_{0,\mathrm{in}}$ are set equal to 101,325 Pa and 288.15 K, respectively. The flow is defined to be normal at the inflow boundary. Turbulence parameters are specified at the inlet section in terms of turbulence intensity and turbulent viscosity ratio, which are set equal to 5% and 10, respectively.

An average relative static pressure $p_{\mathrm{g,out}}$ is imposed at the outflow boundary of the outlet duct, both in the near-choked flow region and in the near-stall region. The outflow pressure is progressively increased in order to reproduce the entire performance trend.

Rotor blades, stator vanes, and end walls are modeled as no-slip, smooth and adiabatic walls. All the simulations refer to the compressor design rotational speed (i.e., 6054 rpm). Furthermore, since only a section of the full geometry is modeled, rotational conformal periodic boundary conditions are applied to the lateral surfaces of the flow domain.

The results presented in this paper are obtained from convergent simulations, with a variation of the residues of the flow and turbulent equations close to zero and all lower than 10^{-4}.

Compressor Performance. The numerical performance curves in terms of total pressure ratio β and adiabatic efficiency η as a function of the mass flow rate m are reported in Fig. 3, along with the best efficiency point. The mass flow rate at the choked-flow condition is equal to 26.48 kg/s.

Particle Model

The solution approach is based on a mathematical model with Eulerian conservation equations for the continuous phase and a Lagrangian frame to simulate a discrete second phase. In this approach, the air flow field is first simulated and then the trajectories of individual particles are tracked by integrating a force balance equation on the particle.

Force Balance. The particle force balance can be written as

$$\frac{d\mathbf{u}_{\mathrm{p}}}{dt} = \mathbf{F}_{\mathrm{D}} + \frac{\rho_{\mathrm{p}} - \rho}{\rho_{\mathrm{p}}}\mathbf{g} + \mathbf{F}_{\mathrm{L}} + \mathbf{F} \tag{1}$$

where the left-hand side represents the inertial force per unit mass acting on the particle and $\mathbf{u}_{\mathrm{p}}$ is the particle velocity vector. The first and the second term on the right-hand side are the drag force and the buoyancy force per unit particle mass, respectively, where ρ_{p} is the particle density, ρ is the air density, and $\mathbf{g}$ is the gravity acceleration vector. The third term $\mathbf{F}_{\mathrm{L}}$ refers to the shear-induced lift force per unit mass acting on particles. The last term $\mathbf{F}$ represents additional forces per unit mass on particles, whose significance will be clarified in the following lines of this paragraph.

The general expression for the drag force acting on smooth spherical particles is

$$\mathbf{F}_{\mathrm{D}} = \frac{18\mu}{\rho_{\mathrm{p}} d_{\mathrm{p}}^2}\frac{C_{\mathrm{D}}\mathrm{Re}_{\mathrm{p}}}{24}(\mathbf{u} - \mathbf{u}_{\mathrm{p}}) \tag{2}$$

where μ is the fluid dynamic viscosity, d_{p} is the particle diameter, C_{D} is the drag coefficient, Re_{p} is the particle Reynolds number

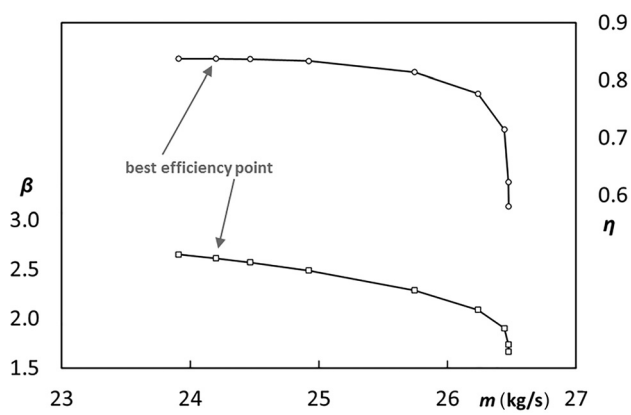

Fig. 3 Compressor performance curves: total pressure ratio and adiabatic efficiency

$$\mathrm{Re}_p = \frac{\rho d_p |\mathbf{u}_p - \mathbf{u}|}{\mu} \tag{3}$$

and $\mathbf{u}$ is the fluid velocity vector.

The drag coefficient C_D is dependent upon the particle Reynolds number. For spherical particles, three different regimes can be identified:

AQ6

- at low particle Reynolds numbers ($\mathrm{Re}_p < 0.1$), the drag coefficient is defined by the Stokes' law, $C_D = 24/\mathrm{Re}_p$ (*viscous* regime);
- for particle Reynolds numbers that are sufficiently large for inertial effects to dominate viscous effects ($10^3 < \mathrm{Re}_p < 2 \times 10^5$), the drag coefficient becomes independent of the Reynolds number, $C_D = 0.44$ (*inertial* regime);
- in the *transitional* region between the viscous and inertial regimes ($0.1 < \mathrm{Re}_p < 10^3$), both viscous and inertial effects are important and the drag coefficient is thus a function of the particle Reynolds number, which must be determined through experiments. The empirical correlation adopted in the present analysis is due to Schiller and Naumann [14]

$$C_D = \frac{24}{\mathrm{Re}_p}\left(1 + 0.15\ \mathrm{Re}_p^{0.687}\right) \tag{4}$$

Small particles in a shear flow field experience a lift force $\mathbf{F}_L$ perpendicular to the direction of relative motion of the two phases. The lift force is most significant in shear layers whose width is comparable to the particle diameter (i.e., boundary layers). The expression for the shear lift force was first obtained by Saffman [15,16] for low Reynolds number flow past a spherical particle. Saffman's expression for the lift force was generalized by Mei and Klausner [17] to a higher range of particle Reynolds numbers. The Saffman–Mei model [12] is applied in this study to calculate the lift force on spherical solid particles.

As stated earlier, Eq. (1) incorporates additional forces $\mathbf{F}$ in the particle force balance that can be important under special circumstances. These additional contributions are (i) forces that arise when modeling the flow in a rotating frame of reference (centrifugal and Coriolis forces), (ii) the force required to accelerate the fluid surrounding the particle (virtual mass force), and (iii) the force applied on the particle due to the pressure gradient in the fluid (pressure gradient force).

The virtual mass and pressure gradient forces are only significant when the fluid density is comparable to or greater than the particle density. Since the numerical simulations involve the transportation of solid particles in a gaseous flow, the density ratio ρ/ρ_p is much smaller than unity. For this reason, the virtual mass and pressure gradient forces are not considered in the force balance.

Particle Turbulent Dispersion. The turbulent dispersion of particles in the fluid phase is predicted by using a stochastic tracking model, which includes the effect of instantaneous turbulent velocity fluctuations on the particle trajectories. The instantaneous fluid velocity is decomposed into mean and fluctuating components, the latter governing each particle's turbulent dispersion. Particles injected from a single point may follow separate trajectories due to the random nature of the instantaneous fluid velocity. By computing the trajectory in this manner for a sufficient number of particles, the random effects of turbulence on particle dispersion can be included.

The model of turbulent dispersion of particles used in this investigation is due to Gosman and Ioannides [18]. In this model, the fluctuating velocities are assumed to possess a Gaussian probability distribution. This model also assumes that a particle is always within a single turbulent eddy, which has a characteristic fluctuating velocity, lifetime, and length. When a particle enters the eddy, the fluctuating velocity for that eddy is added to the local mean fluid velocity to obtain the instantaneous fluid velocity. The turbulent fluid velocity is assumed to prevail as long as the particle/eddy interaction time is less than the eddy lifetime and the displacement of the particle relative to the eddy is less than the eddy length. If either of these conditions is exceeded, the particle is assumed to be entering a new eddy with new characteristics. The eddy fluctuating velocity, length, and lifetime are calculated based on the local turbulent kinetic energy k and its dissipation rate ε.

Particle Injection. Particle injections take place on the previously solved air flow field, with the compressor operating at the best efficiency point. Particles are released at the same local velocities as the air flow from the compressor inlet section, with equally spaced randomly positioned injection points. The uniform distribution of injection points allows the realization of a uniform particle injection from the inlet section. In every analysis, the total number of tracked particles is 3×10^6. This number of particles is selected in order to satisfy the statistical independence of the results, since turbulent dispersion is modeled based on a stochastic approach. Moreover, it is assumed that particles do not affect the fluid flow (one-way coupling) as the particle's volume fraction is very low ($\ll 10\%$).

Particles are spherical and nondeformable. The particle density ρ_p is set equal to $2560\,\mathrm{kg/m^3}$ and the variation of the particle diameter d_p is in the range of 0.15–1.50 μm, while the Stokes number, St, calculated at the inlet section of each cascade

$$\mathrm{St} = \frac{\rho_p d_p^2}{18\mu}\frac{U_1}{d_h} \tag{5}$$

is in the range of 0.0001–0.02. In Eq. (5), U_1 is the averaged fluid velocity at the cascade inlet section and d_h is the hydraulic diameter for the cross section. Every analysis refers to injections having particles with the same diameter, the same material, and therefore, the same Stokes number. The injection data are summarized in Table 1.

Particle-Wall Interaction. For the calculation of particle rebound velocity and direction, a specific particle-wall interaction model is implemented by the authors using a Fortran routine. In this model, which is imposed on rotor blades, stator vanes, and end walls, the normal and tangential restitution coefficients are defined in agreement with Forder et al. [19], as a function of particle wall impact angle α. In a general application, restitution coefficients could depend on (i) impact velocity, (ii) pressure, and (iii) temperature [20]. In this case, only velocity could represent an obstacle to the correct representation of the particle bounce. As stated earlier, the restitution coefficients used in this study are obtained from Forder et al.'s work [19] in which an oilfield control valve is studied with a flow velocity almost equal to 80 m/s. This velocity value determines the validity of assuming the restitution coefficients independent from the velocity.

The turbulence model plays a key role in the resolution of particle trajectories near the wall. Tian and Hamadi [21] highlight the effect of a different turbulence model on the velocity deposition for particles in a horizontal and vertical duct. The authors report an extensive sensitivity analysis of the relationship between turbulence models, mesh refinement close to the wall and particle dimensions expressed by the nondimensional particle relaxation time τ^+, defined as

$$\tau^+ = \frac{(\rho_p/\rho) d_p^2 u_t^2}{18\nu^2} \tag{6}$$

where ν is the fluid kinematic viscosity, u_t is the shear velocity

$$u_t = \sqrt{\frac{\tau_w}{\rho}} \tag{7}$$

and τ_w is the wall shear stress.

As previously mentioned, the turbulence model used for all the analyses is the standard k–ε and near-wall effects are modeled by means of scalable wall functions. In order to assess the suitability of this turbulence model to study particle deposition in the considered axial compressor, numerical simulations are performed on the vertical duct test case described by Tian and Hamadi [21]. This analysis, whose results are reported in Appendix A, shows that the k–ε turbulence model with scalable wall functions overpredicts the deposition velocity for particles in *Brownian* ($\tau^+ < 10^{-2}$) and *transition* ($10^{-2} < \tau^+ < 10$) regions, and it does not allow the estimation of the real trend of the particle velocity deposition in these regions. On the contrary, in the inertial ($\tau^+ > 10$) region, the predicted trend of the deposition velocity curve is in agreement with the other results.

As can be seen in Table 1, the nondimensional particle relaxation time τ^+ for the simulations presented in this paper is in the range 1–186, which corresponds to the transition and inertial regions in accordance with [21]. For this reason, the k–ε turbulence model with scalable wall functions is considered suitable for studying the deposition phenomenon that occurs in the compressor under examination.

Particle Behavior at Rotor/Stator Interface. Since the compressor simulations are carried out in a steady multiple reference frame, with mixing plane interfaces between stationary and rotating cascades, a computational strategy is required to simulate the relative clocking of particles with the rotor blade as they enter the rotating frame.

According to the adopted strategy, when a particle crosses a mixing plane interface, it enters the new cascade at a location characterized by the same radial coordinate and a randomly assigned circumferential coordinate and its velocity is rotated accordingly [12]. This is in addition to change in the relative velocity that occurs due to the particle changing to a new frame of reference. This strategy is analogous to the "preserved" method used by Zagnoli et al. [22] in steady mixing plane calculations for studying microparticle deposition in the first stage of a high-pressure turbine.

Furthermore, when a particle reaches a periodic boundary, it emerges at the new periodic location and the particle's velocity is rotated accordingly [12].

Results

Starting from the analysis of the location and the kinematic characteristics of particle impacts on the compressor blades, the zones characterized by a high probability of particle deposition are identified by means of the sticking probability calculation.

Numerical Model Validation. In their previous work [23], the authors analyzed the microparticle trajectories in the first-stage rotor of the subsonic axial compressor under investigation, in order to discover which blade zones are affected by particle impact and adhesion. The particle distribution pattern found on the blade surface is confirmed by the experimental data on the distribution of foulants on a dry airfoil surface obtained by Kurz et al. [24]. The numerical simulations in Ref. [23] were carried out using the commercial flow solver ANSYS FLUENT with a stochastic Lagrangian tracking method for particle trajectory calculations. The standard k–ε turbulence model with standard wall functions was used in steady frozen rotor calculations.

On the basis of the particle impact location results reported in Ref. [23], comparative simulations of particle ingestion are performed for the isolated first-stage rotor cascade considering four different particle diameters (0.15 μm, 0.50 μm, 1.00 μm, and 1.50 μm). All the calculations refer to the air mass flow rate considered in Ref. [23], equal to 24.26 kg/s. In this way, the flow conditions within the individually simulated rotor match those resulting from the simulations in Ref. [23].

Only a portion of the particles injected from the inlet section of the rotor cascade impacts on the blade. For comparison among the studied cases, the ratio η_{hit} can be used. η_{hit} is defined as the ratio between the number of particles that hit the blade and the total number of injected particles. The trend of η_{hit} as a function of the particle diameter d_p is shown in Fig. 4.

It is possible to observe that the percentage of particles that hit the blade surface increases with the particle diameter. The predicted η_{hit} values are lower with respect to those reported by Suman et al. [23] in the whole range of particle diameters explored, even though the impact trend is the same.

Regarding the particle impact location on the blade surface, Fig. 5 shows the trends of the impacting particles on the blade as a function of the particle diameter. The η_{hit} values for the pressure side, $\eta_{\text{hit,PS}}$, and the suction side, $\eta_{\text{hit,SS}}$, refer to the percentage of particles that hits the pressure side or suction side compared to the total number of injected particles.

It can be seen that, by increasing the particle diameter, the number of particles that hit the pressure side increases. The calculated $\eta_{\text{hit,PS}}$ values are lower with respect to those provided by Suman et al. [23] for all the considered particle diameters, even though the $\eta_{\text{hit,PS}}$ trend is the same. For the suction side, the number of

Table 1 Injection data

			Stokes number, St				Nondim. relax. time, τ^+			
	1		0.15	0.50	1.00	1.50	0.15	0.50	1.00	1.50
STAGE	First	ROTOR	1×10^{-4}	2×10^{-3}	7×10^{-3}	1×10^{-2}	1	12	47	106
		STATOR	1×10^{-4}	2×10^{-3}	6×10^{-3}	1×10^{-2}	1	8	33	73
	Second	ROTOR	2×10^{-4}	2×10^{-3}	7×10^{-3}	2×10^{-2}	1	13	52	118
		STATOR	1×10^{-4}	2×10^{-3}	7×10^{-3}	1×10^{-2}	1	9	35	79
	Third	ROTOR	2×10^{-4}	2×10^{-3}	7×10^{-3}	2×10^{-2}	1	14	57	129
		STATOR	2×10^{-4}	2×10^{-3}	7×10^{-3}	2×10^{-2}	1	9	37	84
	Fourth	ROTOR	2×10^{-4}	2×10^{-3}	7×10^{-3}	2×10^{-2}	1	15	61	137
		STATOR	2×10^{-4}	2×10^{-3}	7×10^{-3}	2×10^{-2}	1	10	40	90
	Fifth	ROTOR	2×10^{-4}	2×10^{-3}	8×10^{-3}	2×10^{-2}	1	16	66	147
		STATOR	2×10^{-4}	2×10^{-3}	8×10^{-3}	2×10^{-2}	1	11	43	96
	Sixth	ROTOR	2×10^{-4}	2×10^{-3}	8×10^{-3}	2×10^{-2}	2	18	71	159
		STATOR	2×10^{-4}	2×10^{-3}	8×10^{-3}	2×10^{-2}	1	12	46	105
	Seventh	ROTOR	2×10^{-4}	2×10^{-3}	9×10^{-3}	2×10^{-2}	2	19	76	171
		STATOR	2×10^{-4}	2×10^{-3}	9×10^{-3}	2×10^{-2}	1	13	51	114
	Eighth	ROTOR	2×10^{-4}	2×10^{-3}	1×10^{-2}	2×10^{-2}	2	21	83	186
		STATOR	2×10^{-4}	3×10^{-3}	1×10^{-2}	2×10^{-2}	1	14	56	127

impacts taking place on the blade decreases from $d_p = 0.15$ μm to $d_p = 0.50$ μm and then increases to $d_p = 1.50$ μm. An analog $\eta_{hit,SS}$ trend is found by Suman et al. [23], even if the number of particles that hit the suction side decreases from $d_p = 0.15$ μm to $d_p = 1.00$ μm and then increases to $d_p = 1.50$ μm.

Overall, the results related to particle impacts on the first-stage rotor blade are in line with those presented in Ref. [23]. For this reason, the numerical model developed in the present work is considered reliable for analyzing particle deposition in the multistage compressor under examination.

Impact Analysis. The modules of the particle impact velocity v_i are reported in Figs. 6–9 for the compressor blades. Each figure refers to a single particle diameter. The velocity values refer to the vector sum of the three velocity components along the coordinate axes at the impact point on the blade surface. Each dot, which represents a single particle that hits the blade, is colored by the impact velocity and is superimposed with respect to the mesh node that provides the blade shape.

The results show that microparticles tend to follow the flow by impacting at full span. The effects of centrifugal forces on particle trajectories are not visible, since the considered particle diameters are too small, as observed by Tabakoff et al. [25]. In their work, the authors analyze the effect of particle size on particle dynamics and blade erosion in an axial flow turbine. The computational analysis shows that the trajectories of the smallest particles ($d_p = 2.50$ μm) do not deviate from the streamlines. The deviation appears for a particle diameter equal to 15 μm.

From a fouling point of view, the most interesting results refer to the case with the smallest particles (Fig. 6). For this case in fact, even though the number of particles that hit the blade surface is the smallest (see Fig. 4), the particles are present both on pressure side and suction side. The impact patterns show that there is not a blade area free from particle impact and, as a consequence, the blade surface could be completely affected by deposits.

These overall impact patterns are directly related to the fluid dynamic phenomena that characterize the three-dimensional flow field of the compressor. In particular, as reported by Fottner [26], clearance vortices and corner vortices determine three-dimensional flow structures of the flow field inside an axial compressor. For the rotor blades, the tip leakage flow determines the impact velocity peaks that take place at the blade tip area, while the low impact velocities at the rear part of the blade on the suction side are due to the hub-corner separation. The stator vanes show different impact velocity patterns. The impact velocity assumes the lowest values at the rear part of the vane on the suction side, where the casing-corner separation exists. The impact velocity peaks that take place at the hub are determined by the hub leakage flow.

Furthermore, it can be noticed that the particles that hit the suction side are especially concentrated at the leading edge of the blade. The impact velocity is not the only parameter needed to determine particle adhesion on the blade surface. Particle adhesion is due to a combination of different effects, but the most important parameters are the normal v_n and tangential v_t impact velocity components. Therefore, the particle impact angle α, which is the angle between the surface normal vector and the impact velocity vector, is analyzed in order to better understand the kinematic characteristics of particle impact.

In Figs. 10–13, the particle impact angle is reported by means of colored particle plots for the compressor blades. Each figure refers to a single particle diameter.

As can be seen, nearly all of the particle impacts are characterized by a value of the impact angle close to 90 deg (i.e., particles are tangential to the blade surface). Smaller values of the impact angle are determined on the suction side of both rotor blades and stator vanes by the hub-corner separation and the casing-corner separation, respectively. At the leading edge, the stagnation of the flow results in normal impacts ($\alpha \approx 0$ deg).

Adhesion Analysis. The particles that stick to the compressor blades are shown in Figs. 14–17 by using black dots. Each dot represents a stuck particle (i.e., a particle for which the sticking probability is greater than 0.5). Each figure refers to a single particle diameter.

The quantitative analysis of particle adhesion on the compressor blades is performed by using the experimental results provided by Poppe et al. [27], in which particle velocities, materials, and dimensions are among the most similar to those of particles causing the fouling phenomenon. As the authors previously showed in Refs. [23] and [28], starting from the experimental sticking probability trends reported in Ref. [27], it is possible to define representative trends for the correlation between the normal impact velocity and the sticking probability. Smaller particles are found to have a wider range of normal impact velocity for which particle impact with the blade surface becomes (with a high probability) a permanent adhesion. The aforementioned correlations are used to calculate the sticking probability for each particle that impacts on the surface by using the normal impact velocity, whose modules are shown in Appendix B for the compressor blades.

Because of the particle-wall interaction settings, particles bounce on rotor blades, stator vanes, and end walls following the rules imposed by the restitution coefficients. In the literature, some studies can be found on the effects of the particle bounce especially related to erosion phenomena [8]. Bouncing particles possess high kinetic energy that decreases by an order of magnitude during the first impact [27]. Such a phenomenon implies that

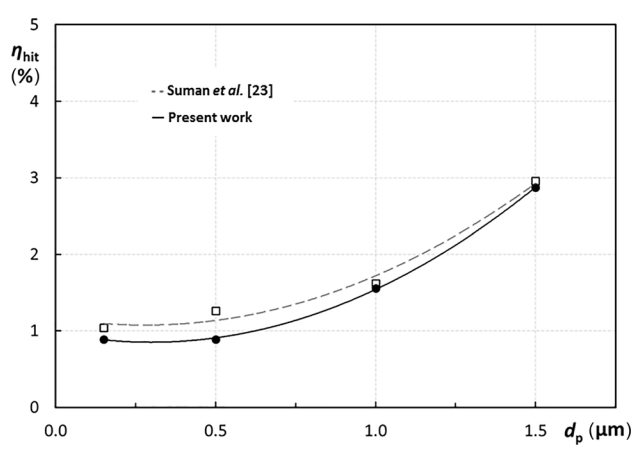

Fig. 4 Capture efficiency versus particle diameter for the isolated first-stage rotor

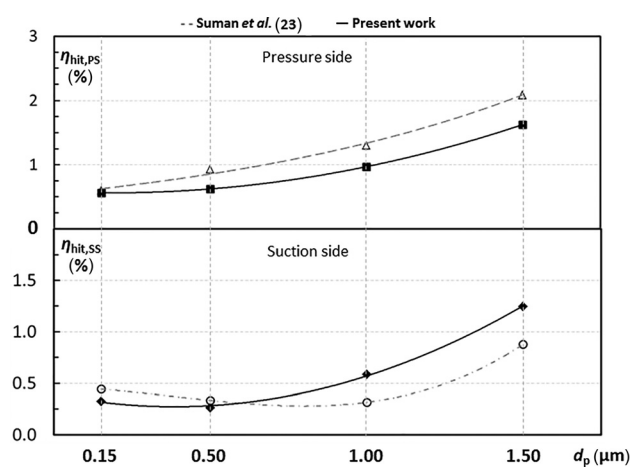

Fig. 5 Particle impact distributions for the isolated first-stage rotor

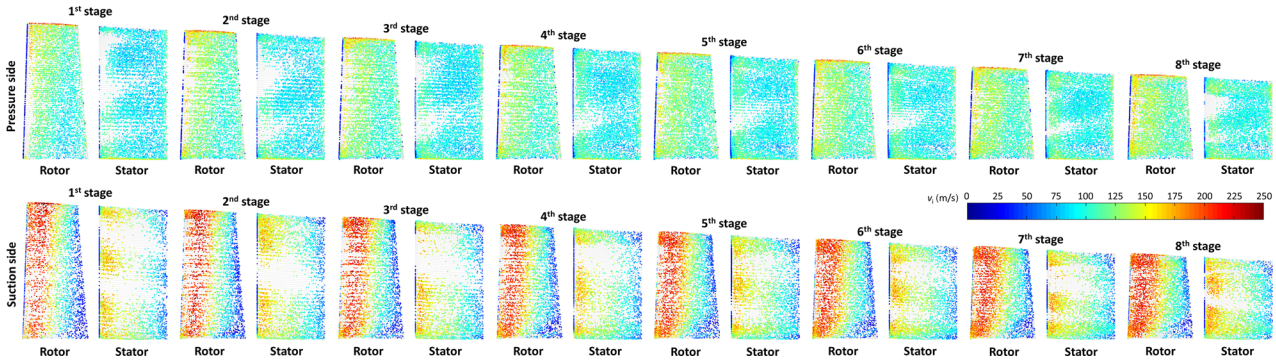

Fig. 6 Particle impact velocity, $d_p = 0.15\ \mu$m

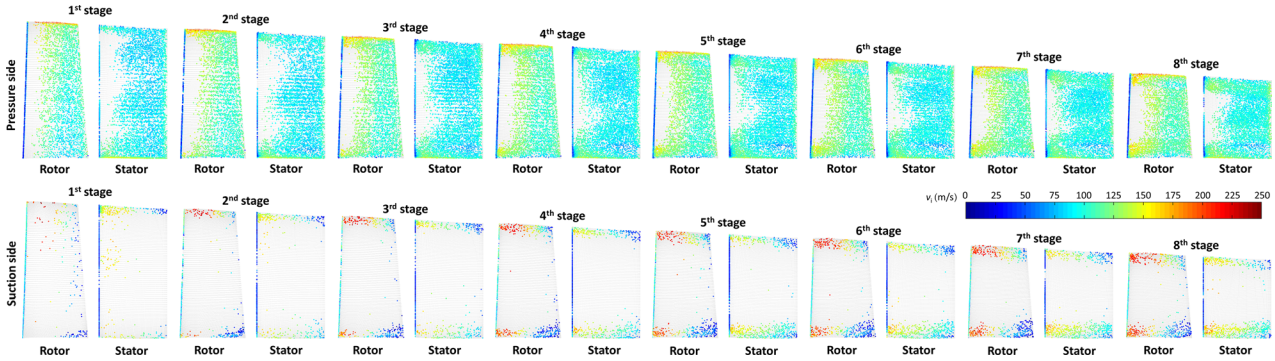

Fig. 7 Particle impact velocity, $d_p = 0.50\ \mu$m

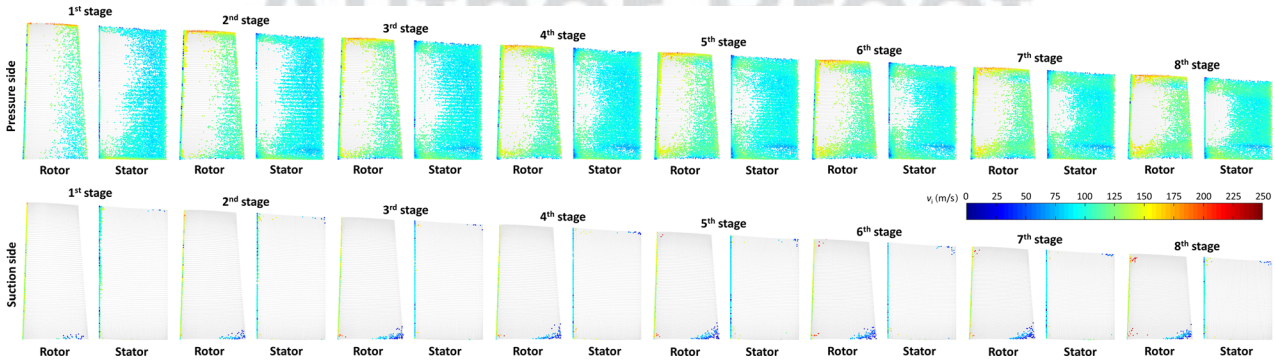

Fig. 8 Particle impact velocity, $d_p = 1.00\ \mu$m

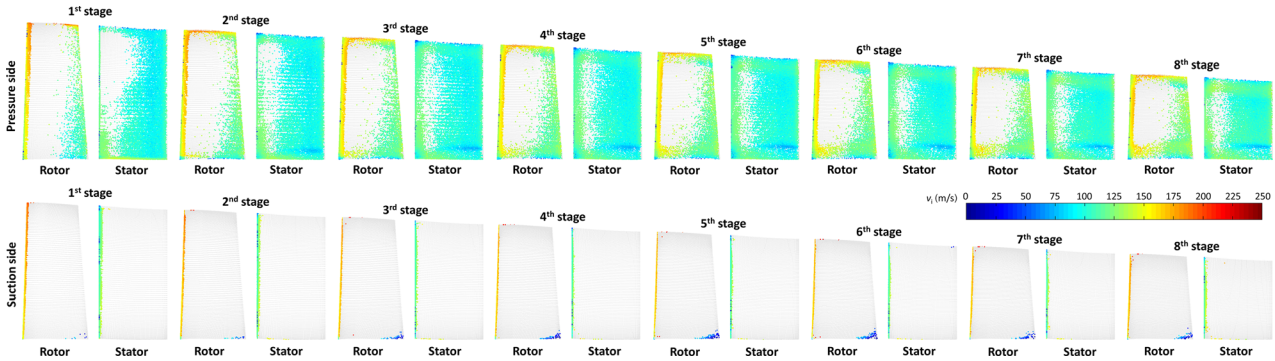

Fig. 9 Particle impact velocity, $d_p = 1.50\ \mu$m

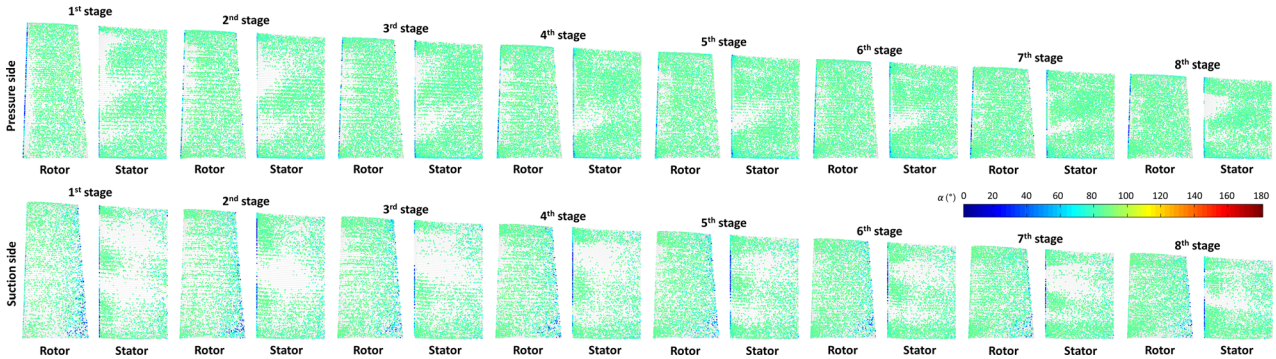

Fig. 10 Particle impact angle, $d_p = 0.15\ \mu$m

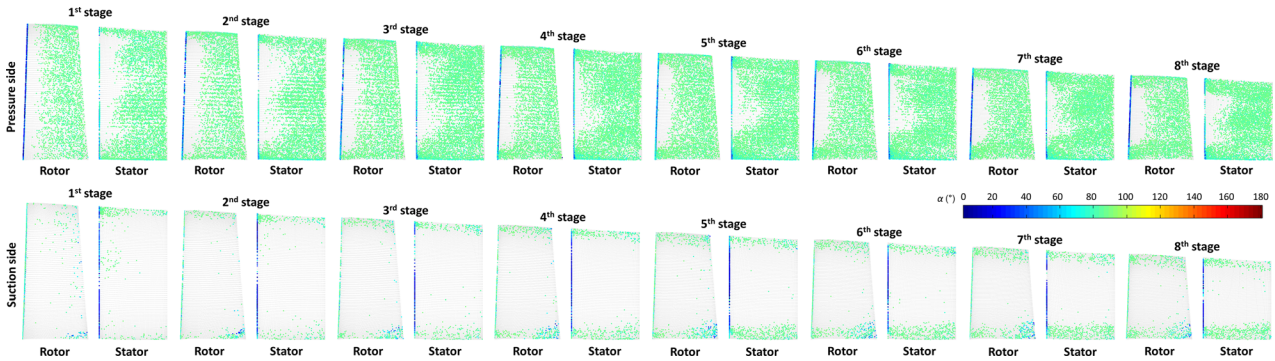

Fig. 11 Particle impact angle, $d_p = 0.50\ \mu$m

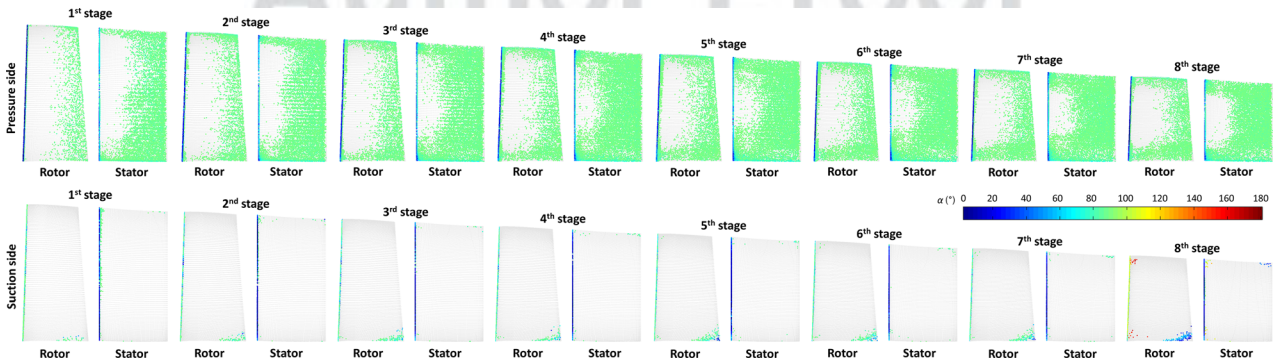

Fig. 12 Particle impact angle, $d_p = 1.00\ \mu$m

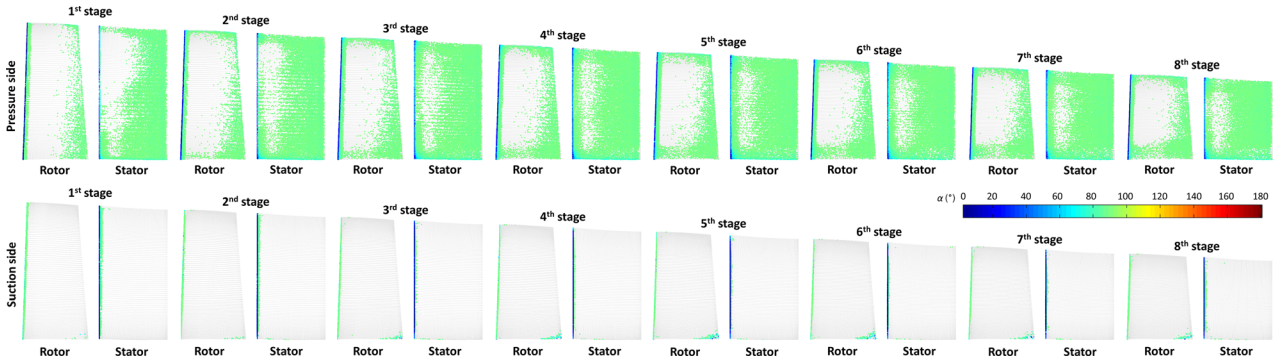

Fig. 13 Particle impact angle, $d_p = 1.50\ \mu$m

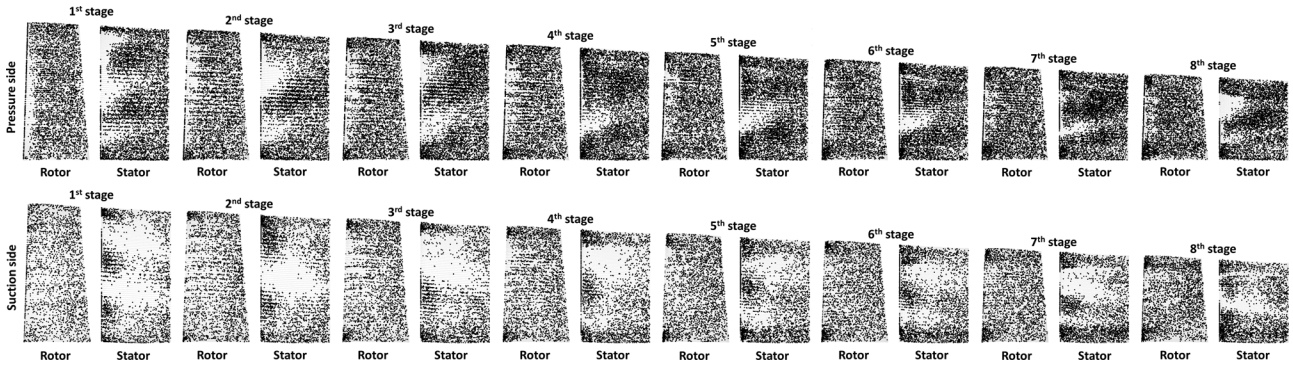

Fig. 14 Particle deposition patterns, $d_p = 0.15\ \mu$m

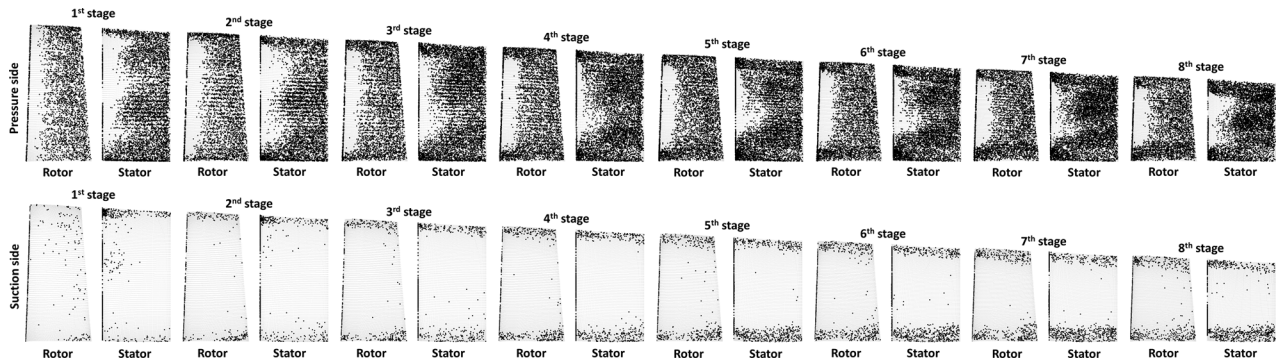

Fig. 15 Particle deposition patterns, $d_p = 0.50\ \mu$m

these particles will not be able to stick during the first contact, but, instead, will be more likely to stick during the second one. In fact, the decrease in kinetic energy is related to the decrease in velocity and, consequently, to an increase in sticking probability. For this reason, the particle adhesion results take into account the particle bounces. More specifically, the bounces of each particle are analyzed in terms of normal impact velocity using a Fortran routine implemented by the authors. The particle is only considered stuck to the surface when the normal impact velocity value allows particle sticking (i.e., the sticking probability is greater than 0.5) and, consequently, the calculation of its trajectory is interrupted. Otherwise, the particle bounces on the surface in accordance with the imposed restitution coefficients.

As can be seen in Figs. 14–17, the deposition zones reflect the impact areas. The smallest particles are able to cover the entire blade surface (pressure and suction sides), even though a small portion of the blade close to the leading edge appears free from deposits. Moving to bigger particles, the suction side and certain zones of the pressure side are less affected by particle adhesion.

The fluid dynamic phenomena previously described strongly influence the deposition patterns. For the rotor blades, the tip leakage flow and the hub-corner separation determine particle adhesion at the blade tip on both sides of the blade and at the rear part of the blade on the suction side. For the stator vanes, the hub leakage flow and the casing-corner separation cause deposits at the hub on both sides of the vane and at the rear part of the vane on the suction side.

Figure 18 shows the trends of the ratio η_{hit} and $\eta_{hit,SP>0.5}$, for particles characterized by a sticking probability greater than 0.5, along the compressor. The particle impact and deposition trends are separately analyzed for the two sides (pressure and suction sides) of rotor blades and stator vanes, in agreement with the investigations reported in the literature [6,7].

In the case of rotor blades, the differences between the values of η_{hit} and $\eta_{hit,SP>0.5}$ are bigger than those obtained for stator vanes. Therefore, the particles that impact on the stator vane surfaces seem to have a greater chance of sticking. This phenomenon is probably due to the influence of the rotor blade speed that determines higher values of particle impact velocity, and

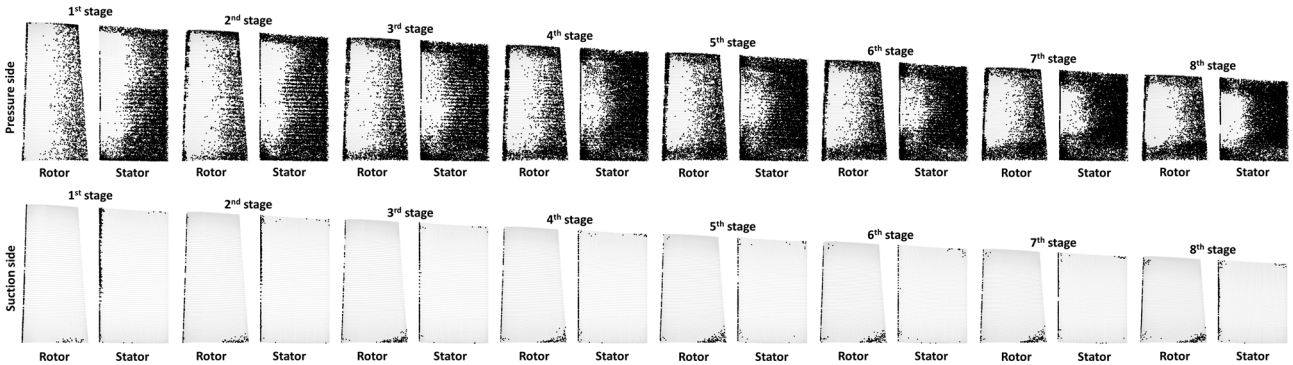

Fig. 16 Particle deposition patterns, $d_p = 1.00\ \mu$m

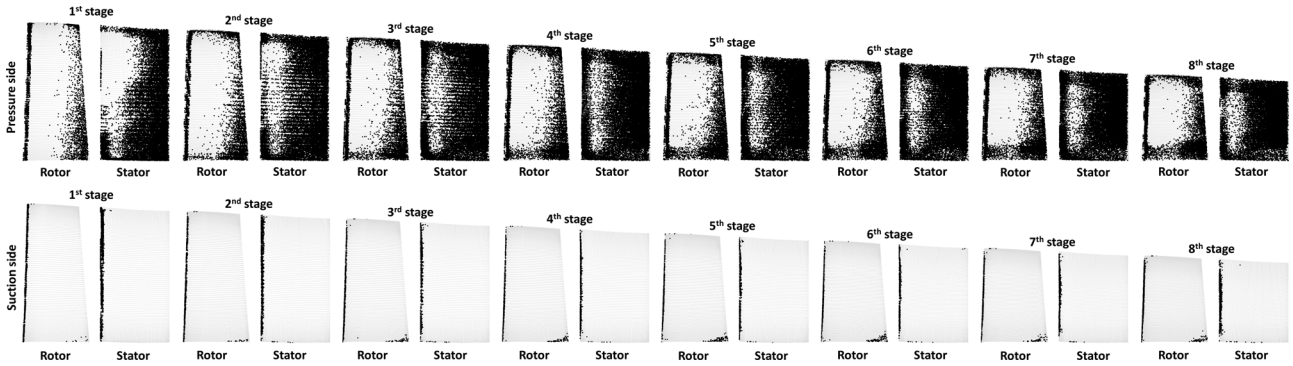

Fig. 17 Particle deposition patterns, $d_p = 1.50\ \mu$m

therefore, lower values of sticking probability. Furthermore, the difference between the values of η_{hit} and $\eta_{hit,SP>0.5}$ increases with the particle diameter. The two percentages are very close to each other only for the smallest particles, showing the high capability of smaller particles to stick to the blade surface. For the suction side, the trend of the ratio $\eta_{hit,SP>0.5}$ highlights a high percentage of particles able to stick for the smallest diameters compared to the total number of particles that hit the suction side. For higher particles, this percentage is very low due to the very low number of particles that reach the suction side.

The impact and deposition trends decrease according to the stages. The front stages appear more affected by particle impact and deposition than the rear ones. This phenomenon is more evident in the case of bigger particles, while for the smallest particles ($d_p = 0.15\ \mu$m) the trends appear quite constant.

The final analysis is related to the distribution of the deposits along the compressor flow path. As mentioned earlier, the impact and deposition trends decrease along the stages, even though this reduction is not comparable with that reported in the literature [6,7]. These fouling detections have revealed that only the first stages are affected by deposits, for which humid conditions play a key role. In Ref. [6], only the first 5–6 stages of 16 are subjected to blade fouling. The deposit masses decrease from the first to the sixth stage, and from the seventh stage, the amount of deposits on the blades is insignificant. In Ref. [7], the experimental tests have shown that the salt deposits were mainly found along the leading edge of the first four stages and on the pressure side of the stator vanes along the hub. The salt deposits were generated by the salt contained in the water droplets and, for this reason, significantly fewer deposits were observed on the rotor blades compared to the

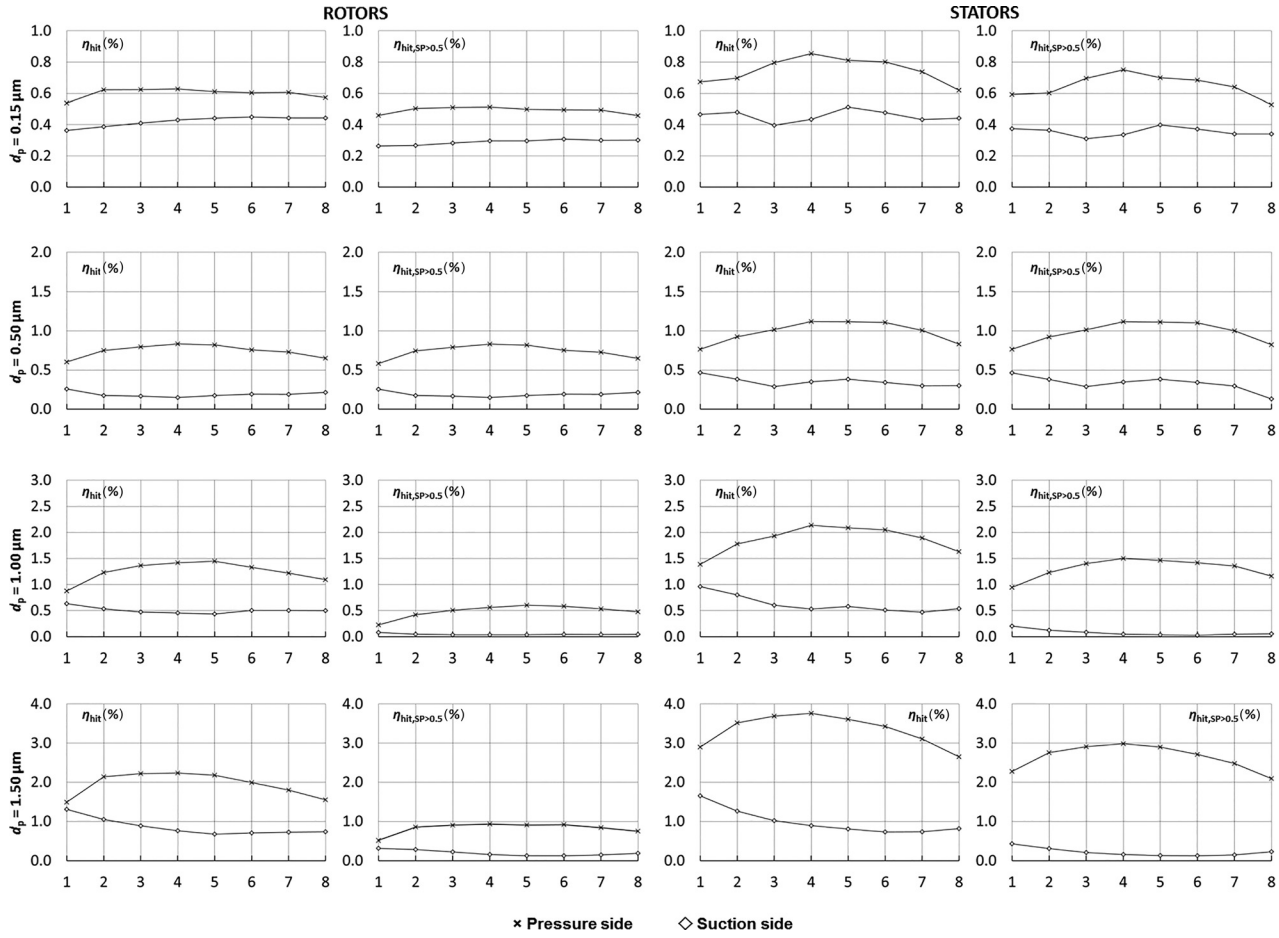

Fig. 18 Trends of the ratio η_{hit} and $\eta_{hit,SP>0.5}$

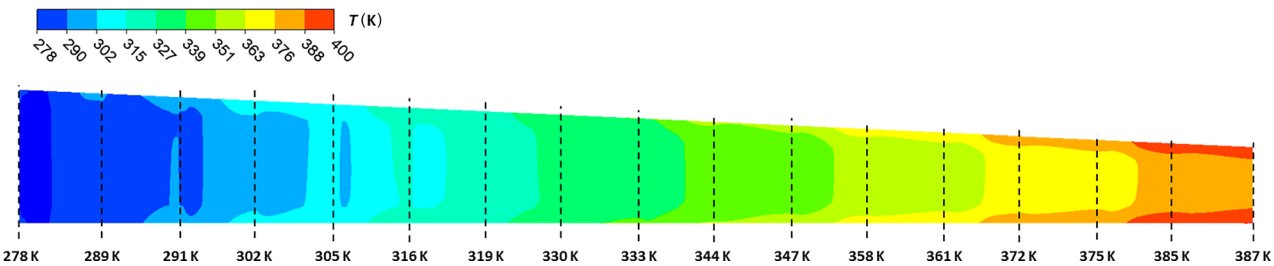

Fig. 19 Static temperature evolution along the compressor

stator vanes. In this case, the cleaning effects of the water droplets on the rotor surface are clearly present. The amount of deposits obtained by Syverud et al. [7] on the stator vanes matches with those reported in Ref. [6], proving the influence of water droplets. This mechanism is well described in the literature [29–31]. The air flow accelerates in the vicinity of the first rotor and the static temperature decreases immediately. If condensation occurs (in cases where the air humidity is high, the air temperature could be lower than the saturation temperature), the dust particles serve as nuclei for condensation of the water vapor and become damp, which speeds up the process of forming deposits. When impinging, the droplets are deformed and splashed over the entire blade surface, generating favorable conditions for dust, soot, and salt particle sticking. During the course of compression, the air becomes warmer and drier, which leads to a reduction in the fouling in the rear cascades.

To support this, Fig. 19 reports the evolution of the static temperature through the stages. At the first rotor inlet, the static temperature decreases to 278 K. In actual operation, this temperature, coupled with an air relative humidity equal to 80%, determines water vapor condensation [29]. From the second stage, the air becomes warmer and no condensation occurs. The deposits shown in Fig. 18 are calculated for dry conditions, since the correlations between normal impact velocity and sticking probability, taken from Ref. [27], are obtained in such conditions. This analysis proves that fouling should be studied considering several factors, such as (i) geometry, (ii) flow field through the stages, (iii) particle dynamics, and (iv) adhesion phenomena caused by the presence of a third substance at the particle/surface interface. In this sense, the numerical CFD calculation is able to solve the flow field and continuously compute the particle dynamics and properties along the compressor flow path.

Conclusions

In this paper, several numerical analyses of multistage compressor fouling are performed. Starting from the validation of the numerical particle tracking and deposition using the literature data, the performance, flow field, and particle trajectories are analyzed for a heavy-duty subsonic axial compressor.

The conditions under which particles stick to the blade surfaces are strongly related to the experimental data taken from the literature. These data are obtained for dry conditions of carbide silica submicron particles that impact a smooth silica surface.

Solving the flow field and the particle tracking, the numerical analyses show that the particle impact/adhesion patterns of the compressor stages are very similar to each other. Smaller particles are able to cover both blade sides, while bigger particles are localized on the pressure side and at the leading edge of the blade.

The deposit trends according to the subsequent compressor stages do not reflect the on-field detection reported in the literature. This result is probably due to the model used for particle sticking. In particular, the present work demonstrates how compressor fouling phenomenon is the result of multiple factors such as blade shape, particle dimension, and air flow conditions. The literature regarding on-field fouling detection relates the deposit patterns to the humid conditions in which the compressor operates. In this case, the particle adhesion model is only able to predict particle deposition for dry conditions and, for this reason, the deposit patterns do not closely reflect the actual deposits.

Nomenclature

C = coefficient
d = diameter
$\mathbf{F}$ = force vector
$\mathbf{g}$ = gravity acceleration vector
k = turbulent kinetic energy
m = mass flow rate
p = pressure
Re = Reynolds number
St = Stokes number
t = time
T = temperature
$\mathbf{u}$ = velocity vector
u_t = shear velocity
u_d^+ = nondimensional particle deposition velocity
U = averaged velocity
v = velocity
y^+ = nondimensional distance

Greek Symbols

α = impact angle
β = total pressure ratio
ε = dissipation rate of turbulent kinetic energy
η = efficiency
μ = dynamic viscosity
ν = kinematic viscosity
ρ = density
τ_w = wall shear stress
τ^+ = nondimensional particle relaxation time

Subscripts and Superscripts

D = drag
g = gauge
h = hydraulic
hit = particles that impact a surface
i = impact
in = compressor inlet section
L = lift
n = normal direction
out = compressor outlet section
p = particle
t = tangential direction
0 = total
1 = cascade inlet section

Acronyms

CFD = computational fluid dynamics
PS = pressure side
SP = sticking probability
SS = suction side

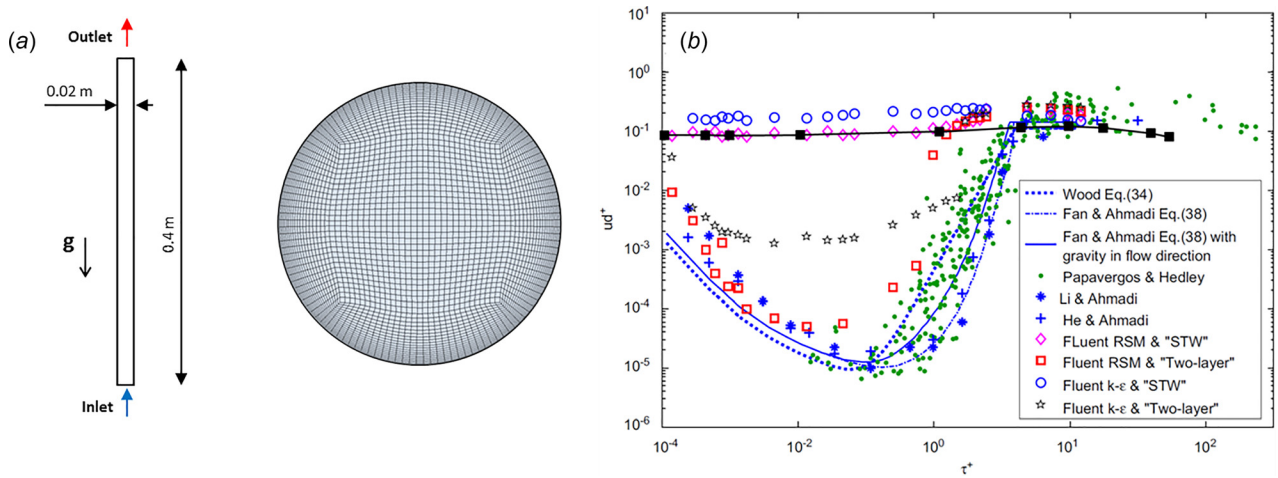

Fig. 20 (*a*) Computational domain and numerical grid, and (*b*) nondimensional particle deposition velocity versus relaxation time [18]

Appendix A: Particle Model Suitability Assessment

In accordance with Tian and Hamadi [18], particle deposition in a vertical duct with gravity in the air flow direction is studied. The diameter of the duct is 0.02 m and its length is equal to 0.4 m. The discretization of the computational domain is realized by means of 2,650,283 hexahedral elements, with 0.5 mm cells in the core region and the first grid points located at 0.05 mm from the wall (Fig. 20(*a*)). The fluid flow is treated as isothermal ($T = 288$ K), incompressible ($\rho = 1.225\,\mathrm{kg/m^3}$) and it is also assumed that the air has a constant dynamic viscosity ($\mu = 1.84 \cdot 10^{-5}$ Pa·s). A fully developed turbulent velocity profile is imposed at the inlet section, with a stream-wise averaged velocity equal to 5.0 m/s, which corresponds to a Reynolds number of 6667. A no-slip boundary condition is applied to the wall, which is considered smooth. A second-order high-resolution advection scheme is used for solving the flow equations.

Spherical particles are injected into the previously solved air flow field. The particle density is kept fixed at $2450\,\mathrm{kg/m^3}$, while the particle diameter is varied in order to reproduce the trend of the deposition velocity curve in the range $10^{-4} < \tau^+ < 10^2$. Particles are released at the same local velocities as the flow from the inlet section, with uniformly distributed injection points. For each particle diameter, the total number of injected particles is 3000. This number of particles is chosen in order to satisfy the statistical independence of the results, as particle turbulent dispersion is predicted through a stochastic model. Since the volume fraction of the particle is very low ($\ll 10\%$), it is assumed that particles do not affect the fluid flow (one-way coupling). The restitution coefficients are set equal to zero on the wall. This implies that particles stick to the wall upon contact.

Particle simulation results are reported in, Fig. 20(*b*), which shows the variation of the nondimensional particle deposition velocity ud+ (calculated according to Tian and Hamadi [18]) as a function of nondimensional particle relaxation time $\tau+$. The numerical results obtained by using the k–ε turbulence model with scalable wall functions (black squares) are superimposed with respect to those provided by Tian and Hamadi [18].

Appendix B: Normal and Tangential Impact Velocity Components

The modules of the particle normal vn and tangential vt impact velocity components are reported in, Figs. 21–24 and 25–28, respectively, for the compressor blades. Each figure refers to a single particle diameter. Each dot, which represents a single particle that hits the blade, is colored by the normal/tangential impact velocity and is superimposed with respect to the mesh node that provides the blade shape.

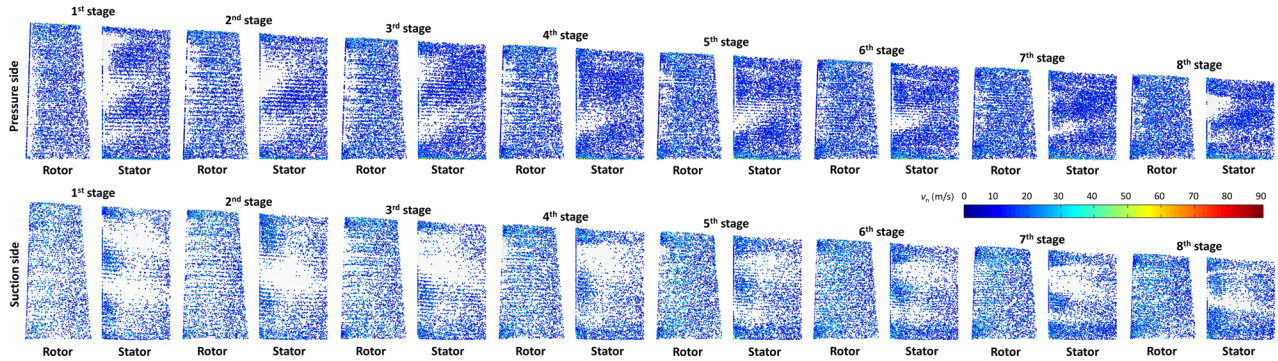

Fig. 21 Particle normal impact velocity, $d_p = 0.15\ \mu$m

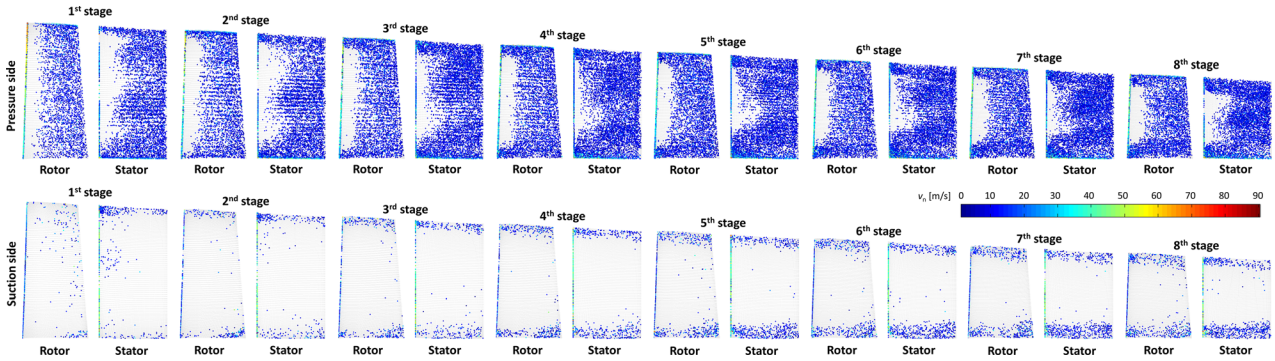

Fig. 22 Particle normal impact velocity, $d_p = 0.50\ \mu$m

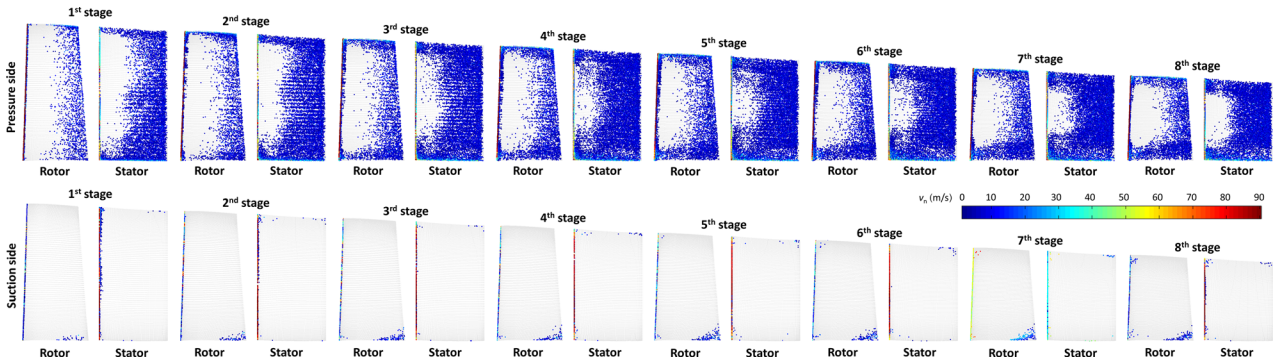

Fig. 23 Particle normal impact velocity, $d_p = 1.00\ \mu$m

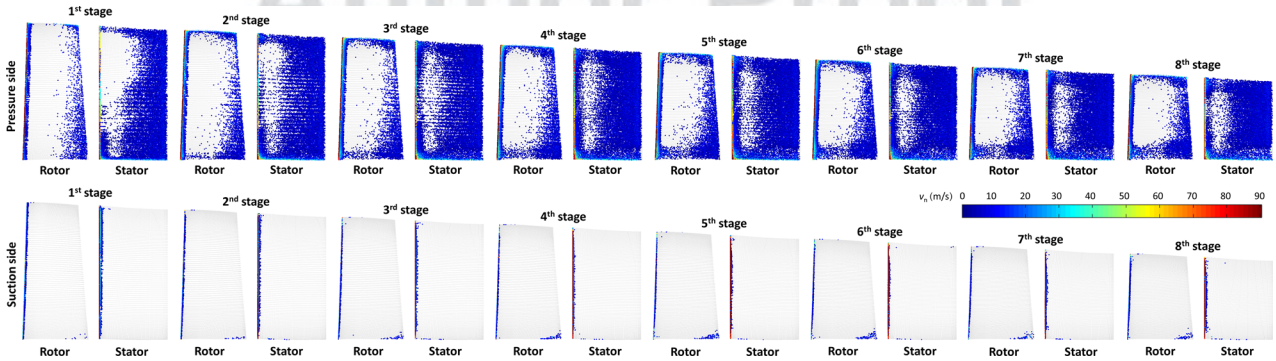

Fig. 24 Particle normal impact velocity, $d_p = 1.50\ \mu$m

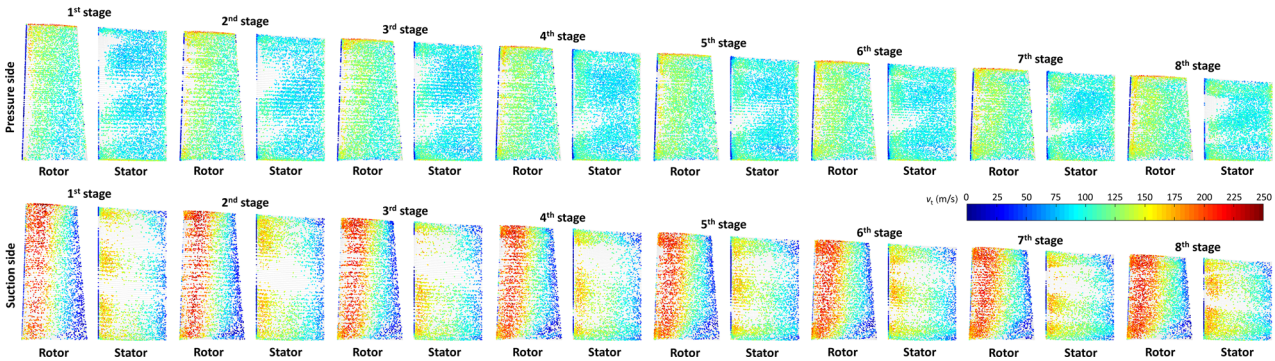

Fig. 25 Particle tangential impact velocity, $d_p = 0.15\ \mu$m

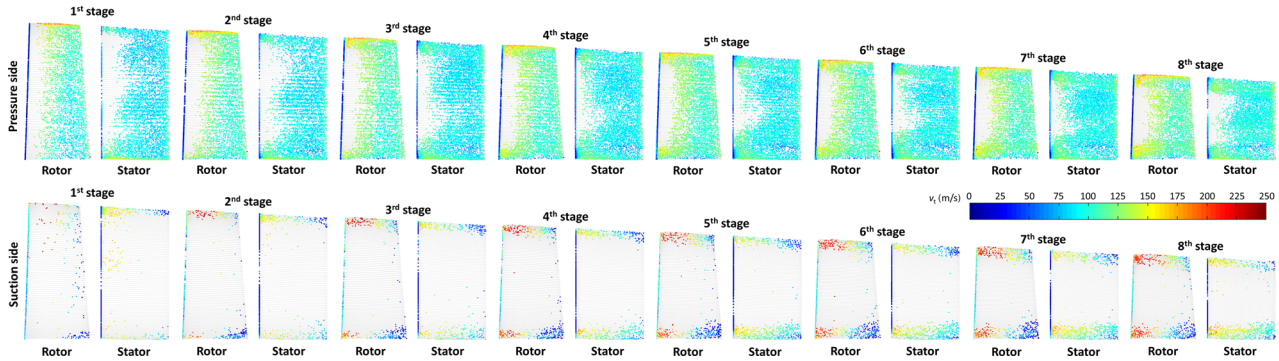

Fig. 26 Particle tangential impact velocity, $d_p = 0.50\ \mu$m

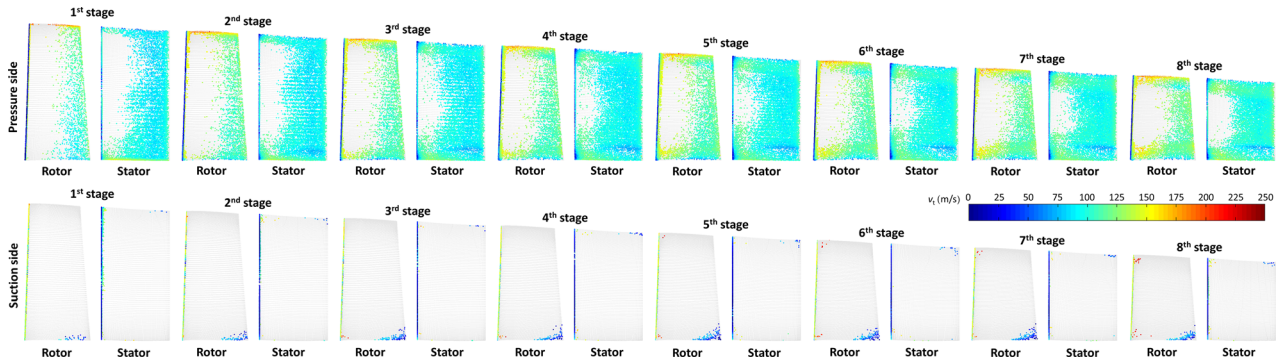

Fig. 27 Particle tangential impact velocity, $d_p = 1.00\ \mu$m

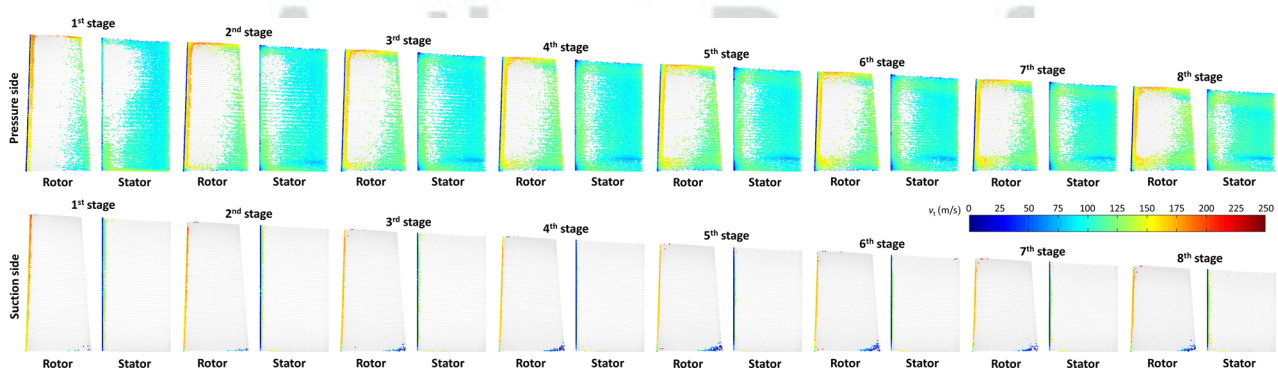

Fig. 28 Particle tangential impact velocity, $d_p = 1.50\ \mu$m

References

[1] Suman, A., Morini, M., Aldi, N., Casari, N., Pinelli, M., and Spina, P. R., 2017, "A Compressor Fouling Review Based on an Historical Survey of ASME Turbo Expo Papers," ASME J. Turbomach., **139**(4), p. 041005.

[2] Kurz, R., Brun, K., Meher-Homji, C., and Moore, J., 2012, "Gas Turbine Performance and Maintenance," 41st Turbomachinery Symposium, Houston, TX, Sept. 24–27, ■.

AQ7

[3] Wilcox, M., Baldwin, R., Garcia-Hernandez, A., and Brun, K., 2010, *Guideline for Gas Turbine Inlet Air Filtration Systems*, Gas Machinery Research Council Southwest Research Institute, San Antonio, TX.

[4] Morini, M., Pinelli, M., Spina, P. R., and Venturini, M., 2010, "Influence of Blade Deterioration on Compressor and Turbine Performance," ASME J. Eng. Gas Turbines Power, **132**(3), p. 032401.

[5] Rodríguez, C., Sánchez, D., Chacartegui, R., Muñoz, A., and Martínez, G. S., 2013, "Compressor Fouling: A Comparison of Different Fault Distributions Using a "Stage-Stacking" Technique," ASME Paper No. GT2013-94010.

[6] Tarabrin, A. P., Schurovsky, V. A., Bodrov, A. I., and Stalder, J.-P., 1998, "Influence of Axial Compressor Fouling on Gas Turbine Unit Performance Based on Different Schemes and With Different Initial Parameters," ASME Paper No. 98-GT-416.

[7] Syverud, E., Brekke, O., and Bakken, L. E., 2007, "Axial Compressor Deterioration Caused by Saltwater Ingestion," ASME J. Turbomach., **129**(1), pp. 119–126.

[8] Suzuki, M., Inaba, K., and Yamamoto, M., 2008, "Numerical Simulation of Sand Erosion Phenomena in Rotor/Stator Interaction of Compressor," J. Therm. Sci., **17**(2), pp. 125–133.

[9] Ghenaiet, A., 2012, "Study of Sand Particle Trajectories and Erosion Into the First Compression Stage of a Turbofan," ASME J. Turbomach, **134**(5), p. 051025.

[10] Aldi, N., Morini, M., Pinelli, M., Spina, P. R., and Suman, A., 2016, "An Innovative Method for the Evaluation of Particle Deposition Accounting for the Rotor/Stator Interaction," ASME J. Eng. Gas Turbines Power, **139**(5), p. 052401.

[11] Saxena, S., Jothiprasad, G., Bourassa, C., and Pritchard, B., 2016, "Numerical Simulation of Particulates in Multistage Axial Compressors," ASME J. Turbomach., **139**(3), p. 031013.

[12] ANSYS CFX, 2015, "Release 16.2, User Manual," ANSYS, Canonsburg, PA.

[13] Cornelius, C., Biesinger, T., Galpin, P., and Braune, A., 2013, "Experimental and Computational Analysis of a Multistage Axial Compressor Including Stall Prediction by Steady and Transient CFD Methods," ASME J. Turbomach., **136**(6), p. 061013.

[14] Schiller, L., and Naumann, A., 1933, "A Drag Coefficient Correlation," Z. Des Vereines Deutscher Ingenieure, **77**(12), pp. 318–320.

[15] Saffman, P. G., 1965, "The Lift on a Small Sphere in a Slow Shear Flow," J. Fluid Mech., **22**(2), pp. 385–400.

[16] Saffman, P. G., 1968, "The Lift on a Small Sphere in a Slow Shear Flow—Corrigendum," J. Fluid Mech., **31**(3), p. 624.

[17] Mei, R., and Klausner, J. F., 1994, "Shear Lift Force on Spherical Bubbles," Int. J. Heat Fluid Flow, **15**(1), pp. 62–65.

[18] Gosman, A. D., and Ioannides, E., 1983, "Aspects of Computer Simulation of Liquid-Fueled Combustors," J. Energy, **7**(6), pp. 482–490.

[19] Forder, A., Thew, M., and Harrison, D. A., 1998, "Numerical Investigation of Solid Particle Erosion Experienced Within Oilfield Control Valves," Wear, **216**(2), pp. 184–193.

[20] Zohdi, T. I., 2005, "Modeling and Direct Simulation of Near-Field Granular Flows," Int. J. Solids Struct., **42**(2), pp. 539–564.

[21] Tian, L., and Ahmadi, G., 2007, "Particle Deposition in Turbulent Duct Flows-Comparisons of Different Model Predictions," J. Aerosol Sci., **38**(4), pp. 377–397.

[22] Zagnoli, D., Prenter, R., Ameri, A., and Bons, J. P., 2015, "Numerical Study of Deposition in a Full Turbine Stage Using Steady and Unsteady Methods," ASME Paper No. GT2015-43613.

[23] Suman, A., Kurz, R., Aldi, N., Morini, M., Brun, K., Pinelli, M., and Spina, P. R., 2015, "Quantitative Computational Fluid Dynamics Analyses of Particle Deposition on a Subsonic Axial Compressor Blade," ASME J. Eng. Gas Turbines Power, **138**(1), p. 012603.

[24] Kurz, R., Musgrove, G., and Brun, K., 2016, "Experimental Evaluation of Compressor Blade Fouling," ASME J. Eng. Gas Turbines Power, **139**(3), p. 032601.

[25] Tabakoff, W., Named, A., and Metwally, M., 1990, "Effect of Particle Size Distribution on Particle Dynamics and Blade Erosion in Axial Flow Turbines," ASME Paper No. 90-GT-114.

[26] Fottner, L., 1989, "Review on Turbomachinery Blading Design Problems," AGARD Lecture Ser., **167**(■), p. ■. AQ8

[27] Poppe, T., Blum, J., and Henning, T., 2000, "Analogous Experiments on the Stickiness of Micron-Sized Preplanetary Dust," Astrophys. J., **533**(1), pp. 454–471.

[28] Suman, A., Morini, M., Kurz, R., Aldi, N., Brun, K., Pinelli, M., and Spina, P. R., 2014, "Quantitative Computational Fluid Dynamic Analyses of Particle Deposition on a Transonic Axial Compressor Blade—Part II: Impact Kinematics and Particle Sticking Analysis," ASME J. Turbomach., **137**(2), p. 021010.

[29] Zaba, T., and Lombardi, P., 1984, "Experience Operation Air Filters Gas Turbine Installations," ASME Paper No. 84-GT-39.

[30] Haskell, R. W., 1989, "Gas Turbine Compressor Operating Environment and Material Evaluation," ASME Paper No. 89-GT-42.

[31] Mezheritsky, A. D., and Sudarev, A. V., 1990, "The Mechanism of Fouling and the Cleaning Technique in Application to Flow Parts of the Power Generation Plant Compressors," ASME Paper No. 90-GT-103. AQ9